Design of a cylindrical corrugated waveguide for a collinear wakefield accelerator

A. Siy,[1,2,*] N. Behdad,[1] J. Booske,[1] G. Waldschmidt,[2] and A. Zholents[2,†]
[1]*University of Wisconsin, Madison, Wisconsin 53715, USA*
[2]*Advanced Photon Source, Argonne National Laboratory, Argonne, Illinois 60439, USA*

(Received 30 May 2022; accepted 7 November 2022; published 7 December 2022)

We present the design of a cylindrical corrugated waveguide for use in the A-STAR accelerator under development at Argonne National Laboratory. A-STAR is a high gradient, high bunch repetition rate collinear wakefield accelerator that uses a 1-mm inner radius corrugated waveguide to produce a 90 MV m^{-1}, 180-GHz accelerating field when driven by a 10-nC drive bunch. To select a corrugation geometry for A-STAR, we analyze three types of corrugation profiles in the overmoded regime with a/λ ranging from 0.53 to 0.67, where a is the minor radius of the corrugated waveguide and λ is the free-space wavelength. We find that the corrugation geometry that optimizes the accelerator performance is a rounded profile with vertical sidewalls and a corrugation period $p \ll a$. Trade-offs between the peak surface fields and thermal loading are presented along with calculations of pulse heating and steady-state power dissipation. In addition to the TM_{01} accelerating mode, properties of the HEM_{11} mode and contributions from higher order modes are discussed.

DOI: 10.1103/PhysRevAccelBeams.25.121601

I. INTRODUCTION

A sub-terahertz accelerator (A-STAR) is being developed at Argonne National Laboratory to reduce the cost and footprint of a future hard x-ray free-electron laser (XFEL) facility [1,2]. A-STAR is a collinear wakefield accelerator (CWA) that uses a cylindrical corrugated waveguide (CWG) as a slow-wave structure, analogous to other CWA configurations [3–8] and drive beam decelerator in CLIC [9]. In operation, a high-charge drive electron bunch passing through the CWA generates an electromagnetic field, known as the wakefield, which accelerates a low charge witness electron bunch following close behind the drive bunch. The ratio of the maximum electric field behind the drive bunch to the maximum electric field within the bunch is known as the transformer ratio $\mathcal{R}$ and is limited to 2 for symmetric drive bunches [10]. The A-STAR design uses a 10-nC asymmetrical drive bunch [10,11] to achieve a transformer ratio of 5 and an accelerating gradient of 90 MV m^{-1}, where the accelerating field is a 180-GHz TM_{01} mode propagating with a group velocity of $0.57c$, where c is the speed of light. The accelerator ends when the drive bunch exhausts almost all of its energy at which point the witness bunch reaches a maximum energy approaching $\mathcal{E}_0(1+\mathcal{R})$, where $\mathcal{E}_0$ is the initial energy of the beam. The entire CWA is composed of many 0.5-m long modules connected in series, as shown in Fig. 1.

The CWA is driven directly by an electron bunch propagating through the structure, making it operationally different from conventional iris loaded linac structures driven by external rf sources. The overall short duration of the rf pulse behind the drive bunch is expected to reduce the rf breakdown rate in the CWG while the growing length of the pulse with distance causes power dissipation in the wall material to increase along the length of the accelerator module. Understanding these effects is critical to the design of a high repetition rate CWA and they will be discussed

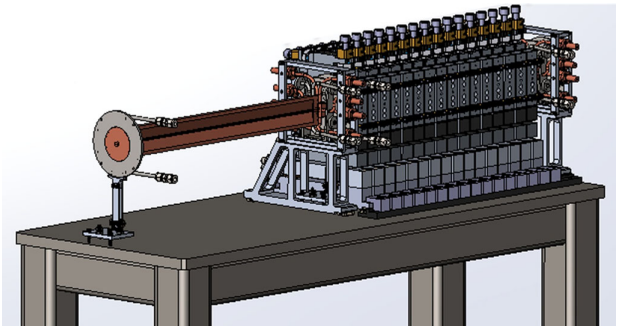

FIG. 1. Two 0.5-m long modules of the CWA connected in series, showing the module on the left with the quadrupole wiggler removed.

*asiy@wisc.edu
†azholents@anl.gov

Published by the American Physical Society under the terms of the Creative Commons Attribution 4.0 International license. Further distribution of this work must maintain attribution to the author(s) and the published article's title, journal citation, and DOI.

further in Secs. V and VI. Creating a large accelerating gradient with a 10-nC drive electron bunch requires the inner radius of the CWG to be small, while manufacturing limitations at the resulting scale require the corrugations/irises to be shallow. These constraints cause the CWG slow-wave structure to have higher group velocity and peak surface fields than iris loaded structures commonly found in the literature. In this paper, we investigate 1-mm inner radius CWG geometries that attempt to minimize power dissipation and peak surface fields, maximizing the bunch repetition rate and accelerating gradient of the CWA. We also attempt to minimize coupling to higher order modes (HOMs) which is the preferred operating condition according to [12]. Using the eigenmode and wakefield solvers in CST Microwave Studio [13], we parametrically characterize a range of corrugation geometries to arrive at the final design of the A-STAR CWG presented in Sec. VIII. Fabrication and testing of the CWG are described in [14] and the vacuum properties of the structure are discussed in [15]. Parameters and variables used throughout paper are given in Table I.

II. CORRUGATION GEOMETRY

The CWG is a round metallic pipe with grooves around the inner circumference of the wall as shown in Fig. 2. The minor radius, a, of the CWG is the distance between the center axis of the waveguide and the tips of the corrugation teeth. Here, we refer to the raised part of the profile as the corrugation tooth and the space between adjacent teeth as the vacuum gap. The radii of the tooth tip and vacuum gap floor are connected by a flat surface called the sidewall and the overall dimensions of the corrugation are small compared to the minor radius a. The shape of the corrugation tooth determines the peak fields and thermal properties of the structure and must be optimized to obtain the maximum accelerating gradient. Figure 3 shows three types of tooth geometries considered in this paper. Each type is a subset of a trapezoidal corrugation with rounded corners, where we have created three separate categories to simplify the presentation of the results.

The first profile is the rectangular corrugation with minimum radii corners Fig. 3(a) which has vertical sidewalls and sharp corners. In this analysis, the corners were given a radius of $r_t = r_g = a/100$ to produce accurate simulation results for the peak surface fields which become very large as the corner radius shrinks. The minimum radii geometry has three degrees of freedom, namely the corrugation tooth width t, vacuum gap g, and depth d. Increasing the corner radius results in the maximum radii profile as shown in Fig. 3(b), which has the same three degrees of freedom but a corner radius as large as possible while preserving the overall depth and period of the profile. Here, $r_t = r_g = \min(t, g, d)/2$, where the min function returns its minimum argument. The final corrugation is the rounded profile with unequal radii tooth tip and vacuum gap, Fig. 3(c). This profile has 4 degrees of freedom: the

TABLE I. Parameters and variables used throughout the paper.

Parameter	
κ	Wakefield loss factor
β_g	Normalized group velocity
v_g	Group velocity
α	Attenuation constant
Q	Quality factor
σ	Electrical conductivity
ξ	Corrugation spacing parameter
ζ	Corrugation sidewall parameter
a	Corrugation minor radius
t	Corrugation tooth width
g	Corrugation vacuum gap
d	Corrugation depth
p	Corrugation period
r_t	Corrugation tooth radius
r_g	Corrugation vacuum gap radius
L	Corrugated waveguide length
F	Bunch form factor
q_0	Drive bunch charge
f_r	Bunch repetition rate
τ	rf pulse decay time constant
δ	Skin depth
P_{rf}	rf pulse power envelope
P	Instantaneous rf pulse power
E_{acc}	Accelerating field
E_{max}	Peak surface E field
H_{max}	Peak surface H field
Q_{diss}	Energy dissipation
P_d	Power dissipation distribution
W	Average thermal power density
ΔT	Transient temperature rise
c	Speed of light
Z_0	Impedance of free space
$\mathcal{E}_0$	Initial beam energy
$\mathcal{R}$	Transformer ratio

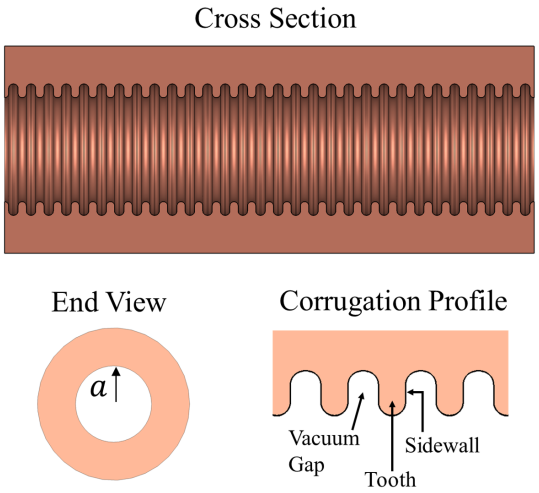

FIG. 2. Cylindrical corrugated waveguide (CWG) with minor radius a. The specific design used in A-STAR has $a = 1$ mm.

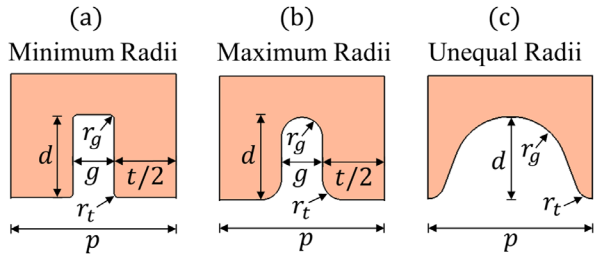

FIG. 3. Dimensions for corrugation types: (a) minimum radii corners, (b) maximum radii corners, (c) rounded with unequal radii corners connected by tangent sidewalls, where $t = 2r_t$ and $g = 2r_g$.

corrugation period p, corrugation depth d, maximum tooth width t, and maximum vacuum gap g. Here, $t = 2r_t$ and $g = 2r_g$ where r_t and r_g are the radii of the tooth tip and vacuum gap contours, respectively. The profile is drawn by connecting the fully rounded corrugation tooth tip and vacuum gap with an inner tangent line, allowing the sidewall angle to vary.

In the parametric analysis that follows, the corrugation dimensions are expressed in terms of the normalized spacing parameter ξ and sidewall parameter ζ defined as

$$\xi = \frac{g - t}{p}, \tag{1}$$

$$\zeta = \frac{g + t}{p}. \tag{2}$$

The spacing parameter ξ determines the spacing between the corrugation teeth and ranges from -1 to 1 for the minimum and maximum radii profiles, where positive values of ξ result in spacing greater than the tooth width and vice versa for negative values. The sidewall parameter ζ controls the sidewall angle of the unequal radii profile, where $\zeta < 1$ leads to tapered sidewalls and $\zeta > 1$ leads to undercut sidewalls. These dependencies are illustrated in Fig. 4.

The condition for vertical sidewalls is $\zeta = 1$ and $d > p/2$. Preventing a self-intersecting geometry requires both the width of the tooth and vacuum gap to be less than the corrugation period, as well as a sufficiently large corrugation depth when $\zeta > 1$ to ensure positive length of the inner tangent line defining the sidewall. These conditions can be expressed as

$$\zeta - 2 < \xi < 2 - \zeta, \tag{3}$$

$$d > \frac{p}{2}\left(\zeta + \sqrt{\zeta^2 - 1}\right) \quad \text{for } \zeta > 1. \tag{4}$$

III. SIMULATION

Electromagnetic simulation of the TM_{01} accelerating mode was performed using the eigenmode solver in CST Microwave Studio [13]. In this analysis, only the fundamental TM_{01} mode was considered since it accounts for the largest portion of the accelerating gradient. It will be shown in Sec. VII that the exclusion of higher order modes (HOMs) is a very good approximation for the corrugated structures under consideration. A tetrahedral mesh and magnetic symmetry planes were used to accurately model the rounded corners of the corrugation and minimize computation time. Since the simulation only considers a single period of the geometry, the run time was short (approximately 1 m on a four-core desktop PC) allowing large parametric sweeps to be run rapidly. The eigenmode solver models the corrugated waveguide as a periodic structure of infinite length by employing a periodic boundary condition derived from beam-wave synchronicity:

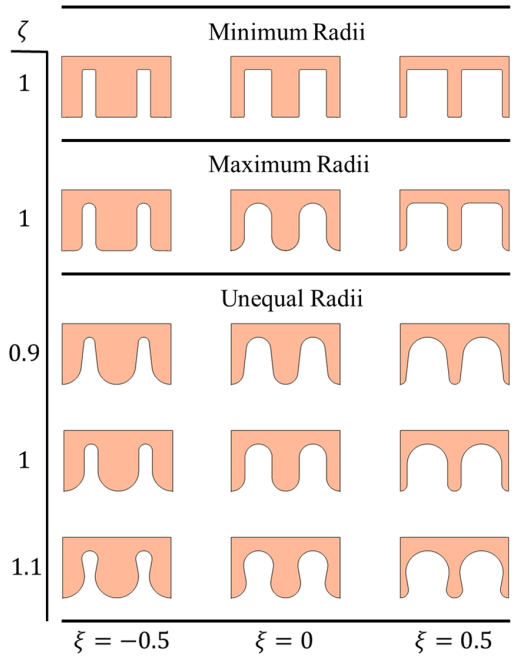

FIG. 4. Corrugation variation with the spacing parameter ξ and sidewall parameter ζ for the minimum radii (top), maximum radii (middle), and unequal radii (bottom) profiles at fixed period and depth.

$$\phi = \frac{360 f p}{c}, \tag{5}$$

where ϕ is the periodic boundary condition phase advance in degrees, f is the frequency of the electromagnetic mode, p is the corrugation period, and c is the speed of light. The electron bunch velocity is considered to be equal to c.

The structures were simulated at three fixed frequencies in order to characterize frequency-dependent behavior of the TM_{01} mode. Throughout the paper, we will refer to results for the simulated frequencies by their respective aperture ratios which we define as a/λ, where a is the minor radius of the CWG and λ is the free-space

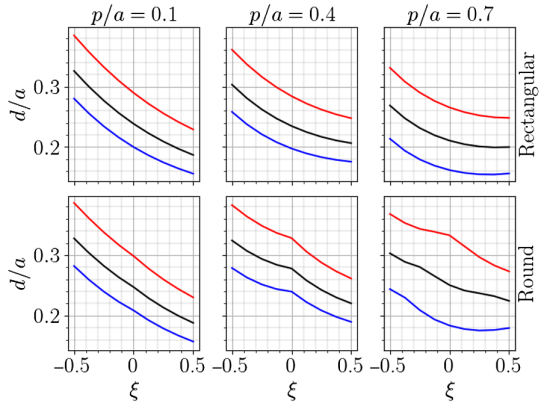

FIG. 5. Corrugation depths calculated for minimum radii corrugations (top) and maximum radii corrugations (bottom) for aperture ratios of $a/\lambda = 0.53$ (red), $a/\lambda = 0.60$ (black), and $a/\lambda = 0.67$ (blue). See Fig. 4 for cell geometries.

wavelength of the synchronous mode. This normalization allows the results to be applied to structures of any size and frequency.

Parametric analysis began by treating the corrugation depth d as a dependent variable determined by the aperture ratio, eliminating it from the parameter sweeps. This was done by using an iterative optimization process to find the corrugation depths required to achieve predetermined frequencies, producing aperture ratios of 0.53, 0.60, and 0.67 for each combination of p, ξ, and ζ in the study. The resulting corrugation depths are plotted in Figs. 5 and 6. In all cases, the corrugation depth decreases with increasing aperture ratio, where shallower corrugations produce

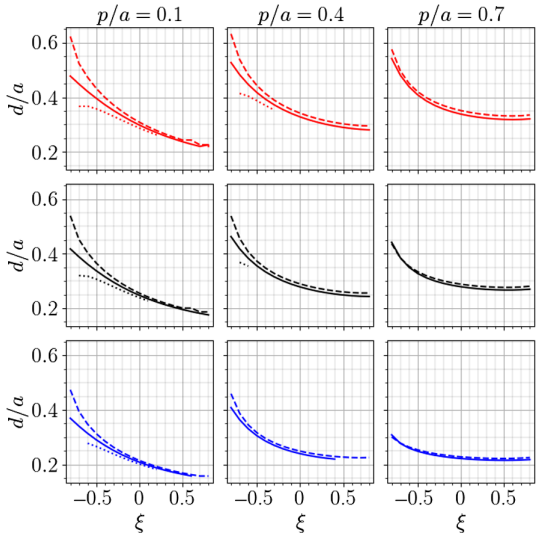

FIG. 6. Corrugation depths calculated for unequal radii corrugations with $\zeta = 0.85$ (dashed), $\zeta = 1.0$ (solid), and $\zeta = 1.15$ (dotted) where the aperture ratios are $a/\lambda = 0.53$ (red), $a/\lambda = 0.60$ (black), and $a/\lambda = 0.67$ (blue). See Fig. 4 for cell geometries.

higher synchronous TM_{01} frequencies. The sidewall parameter ζ is found to modify the effective corrugation depth where reducing ζ has an effect similar to reducing d. Undercut corrugation profiles with $\zeta > 1$ can only be found when the conditions in Eqs. (3) and (4) are satisfied which requires the period and aperture ratio to be sufficiently small. For this reason, the dotted line solutions in Fig. 6 only occur above the set values of the corrugation depth. In the remainder of the analysis, we will pay special attention to the maximum radii corrugation and unequal radii corrugation with $\zeta = 1$ which are good candidates for wakefield acceleration due to their manufacturability and electromagnetic characteristics.

IV. ELECTROMAGNETIC PARAMETERS

Each synchronous eigenmode solution of the periodic structure is characterized by a wakefield loss factor κ, group velocity v_g, and attenuation constant α. These parameters determine how the electron beam interacts with the given mode as well as the propagation characteristics of the corresponding wakefield. In this section, equations for the electromagnetic parameters are defined and applied to the structures found in Sec. III. The results are plotted against the corrugation spacing parameter ξ and period p at each of the three aperture ratios to show how the wave propagation and beam interaction depend on the corrugation geometry and frequency. The loss factor κ describes the energy coupled from a charged particle to the structure and is defined as [16]:

$$\kappa = \frac{V^2/U}{4(1-\beta_g)p}, \tag{6}$$

where V is the induced voltage, U is the stored energy in the unit cell, and β_g is the normalized group velocity v_g/c. The induced voltage is calculated from the time harmonic electric field of the synchronous mode with angular frequency ω as

$$V = \left| \int_0^p E_z(z) e^{j\omega\frac{z}{c}} dz \right|. \tag{7}$$

The group velocity v_g is calculated from the time averaged electromagnetic field power flow P_z, the unit cell length p, and the stored energy U in the unit cell, where P_z is found by integration of the Poynting vector,

$$v_g = \frac{P_z}{U} p. \tag{8}$$

Loss in the structure due to the conductivity of the wall material causes the fields to decay as $\exp(-\alpha z)$, where the attenuation constant α in $\mathrm{Np\,m^{-1}}$ is calculated in terms of the quality factor Q of the unit cell as [17]:

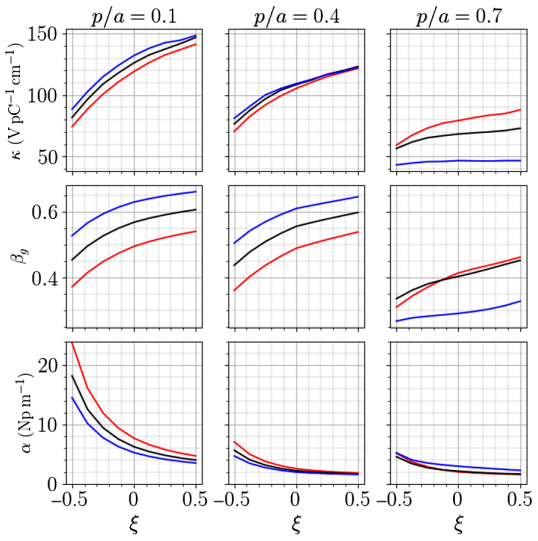

FIG. 7. Loss factor κ, normalized group velocity $\beta_g = v_g/c$, and attenuation constant α for the maximum radii geometry with $a/\lambda = 0.53$ (red), $a/\lambda = 0.60$ (black), and $a/\lambda = 0.67$ (blue). Plotted for a CWG with minor radius $a = 1$ mm and electrical conductivity $\sigma = 4 \times 10^7$ S m^{-1}.

$$\alpha = \frac{\omega}{2Qv_g}. \tag{9}$$

Figure 7 shows how the electromagnetic parameters of the maximum radii corrugation depend on the geometry for a CWG with minor radius $a = 1$ mm and electrical conductivity $\sigma = 4 \times 10^7$ S m^{-1}. The scaling laws derived in Appendix A can be used to project the results to cases with different a and σ. The loss factor κ and group velocity β_g have similar behavior which can be explained in part by the appearance of $(1 - \beta_g)$ in the denominator of Eq. (6). This dependence results in a reduction of κ as the corrugation period increases since β_g goes to zero as the phase advance ϕ approaches the π point of the dispersion curve. Structures with shorter corrugation periods, therefore, produce larger group velocities and wake potentials making it desirable to choose the period as short as possible. As the period shrinks, κ approaches a maximum value, which for a single moded steeply corrugated structure with $d \gtrsim p$ is [18]:

$$\kappa_{\max} = \frac{Z_0 c}{2\pi a^2}, \tag{10}$$

where Z_0 is the impedance of free space. In practical corrugated waveguide designs, the loss factor is always less than $\kappa_{\max}$ due to manufacturing constraints on the minimum corrugation size. In these structures, simulations are required to accurately determine the loss factor.

V. PEAK FIELD MINIMIZATION

The maximum attainable accelerating gradient in the CWA is limited by several factors, including pulse heating and rf breakdown due to the peak surface fields and modified Poynting vector [19–21] exceeding certain threshold values. The corrugated waveguide must be optimized to maximize the accelerating field of the TM_{01} mode while minimizing these factors. Data collected from existing accelerator structures operating up to 30 GHz show that the breakdown rate (BDR), measured in breakdowns per pulse per meter, scales approximately with the magnitude of the peak electromagnetic field $E_{\max}$ as well as the duration of the rf pulse t_p according to [21]:

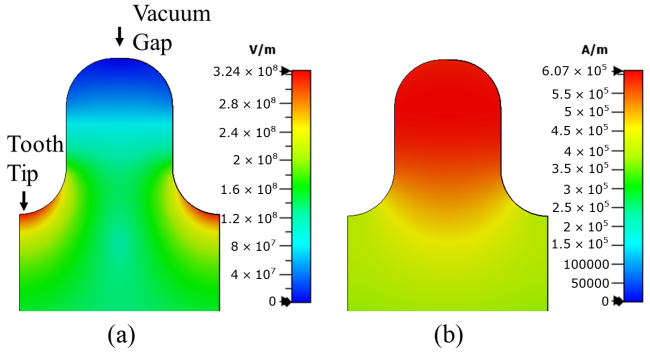

FIG. 8. Peak electric field distribution (a) and magnetic field distribution (b) of the 90 MV m^{-1} TM_{01} accelerating mode in the A-STAR corrugated waveguide.

$$\frac{E_{\max}^{30} t_p^5}{\mathrm{BDR}} = \text{const.} \tag{11}$$

From a design perspective, reducing the BDR is achieved by reducing the peak surface fields and the pulse length. Calculation of the absolute threshold value of the fields that induce breakdown in sub-THz structures is an active area of research [19,22,23] and reliable models have not yet been developed. The modified Poynting vector introduced in [21] has been used to predict rf breakdown in structures operating up to 30 GHz, but there are limited data for its applicability at higher frequencies. For this reason, the BDR and maximum gradient of the CWA must ultimately be determined experimentally. For the purpose of optimization, we choose the peak surface fields $E_{\max}$ and $H_{\max}$ as figures of merit which should be minimized to increase the attainable accelerating gradient. Since some evidence suggests that pulse heating is of fundamental importance to the initiation of rf breakdown in high frequency accelerating structures [24], we give additional weight to the minimization of the peak magnetic surface field. This choice leads to a higher overall thermal efficiency which will be discussed further in Sec. VI.

In evaluating the peak surface fields for the various corrugation geometries, we have normalized the fields over the accelerating gradient given in Eq. (B29) in Appendix B to allow a comparison of the results. Typical electric and magnetic field distributions within the corrugation unit cell are shown in Fig. 8, where the electric field is generally

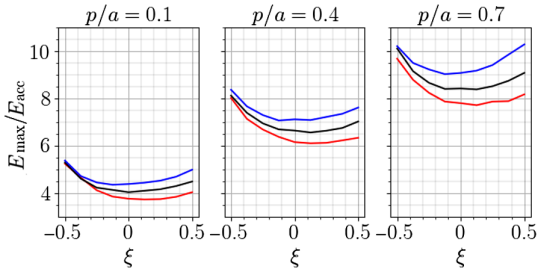

FIG. 9. Normalized peak surface E fields of the minimum radii rectangular corrugation geometry with $a/\lambda = 0.53$ (red), $a/\lambda = 0.60$ (black), and $a/\lambda = 0.67$ (blue).

concentrated around the tooth tip and the magnetic field is highest in the vacuum gap.

The simulation results in Figs. 9 and 10 show that the peak electric and magnetic fields always increase with increasing aperture ratio, meaning higher choices of frequency for the TM_{01} synchronous mode result in higher peak fields for a given accelerating gradient. This observation is consistent with the results reported in [25] and is seen in unequal radii geometries as well. Unlike the rounded geometries, the peak fields of the minimum radii rectangular geometry shown in Fig. 9 have a strong dependence on the corrugation period and higher overall values due to field enhancement at the corrugation corners. At a period of $p/a = 0.4$, the peak electric fields of the minimum radii geometry are roughly double those of the rounded designs making minimum radii rectangular corrugations unsuitable for high gradient CWA structures.

Comparing the maximum radii and unequal radii rounded corrugation peak fields in Figs. 10 and 11, we note that the two geometry types are identical when the spacing parameter $\xi = 0$ and the sidewall parameter $\zeta = 1$. In both structure types, the minimum E_{max} occurs for a negative spacing parameter ξ, corresponding to a

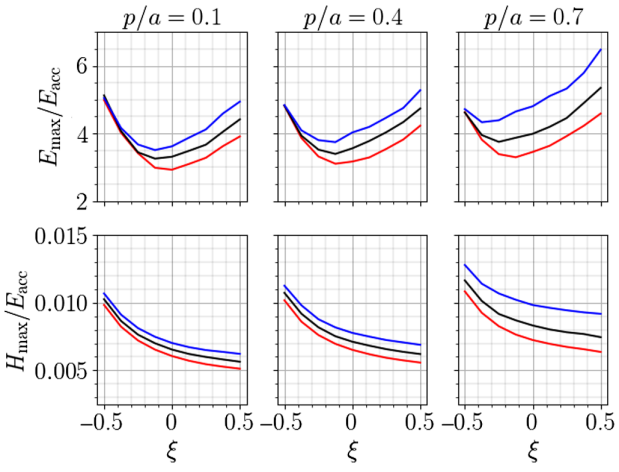

FIG. 10. Normalized peak surface E ($V\,m^{-1}$) and H ($A\,m^{-1}$) fields of the maximum radii corrugation geometry with $a/\lambda = 0.53$ (red), $a/\lambda = 0.60$ (black), and $a/\lambda = 0.67$ (blue).

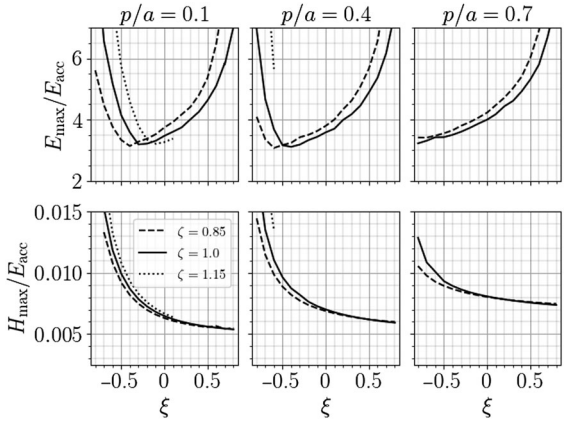

FIG. 11. Normalized peak surface E ($V\,m^{-1}$) and H ($A\,m^{-1}$) fields of the unequal radii corrugation geometry for aperture ratio $a/\lambda = 0.60$ and $\zeta = 0.85$ (dashed), $\zeta = 1.0$ (solid), and $\zeta = 1.15$ (dotted).

corrugation tooth width wider than the vacuum gap. Increasing the corrugation spacing beyond the minimum point decreases H_{max} while increasing E_{max}. The sidewall angle determined by ζ shifts the plots on the ξ axis but does not significantly affect the minimum value of the peak fields. While changing the sidewall parameter offers little to no benefit in reducing the peak fields, the practical implications of using values of $\zeta \neq 1$ have several disadvantages. For tapered corrugations with $\zeta < 1$, the corrugation depth must be greater requiring a thicker vacuum chamber wall and additional manufacturing complexity. Undercut corrugations with $\zeta > 1$ are also impractical to manufacture for the dimensions of interest in a compact wakefield accelerator. For these reasons, we suggest the maximum radii corrugation with ξ close to zero as a good candidate for a wakefield accelerator design. Further refinement of the geometry requires experimental determination of where rf breakdown is most likely to occur in order to reduce the peak fields in those regions.

VI. THERMAL LOADING

Thermal loading of the corrugated waveguide places a limit on the maximum repetition rate f_r of the accelerator, where f_r is the number of bunches injected into the structure per second. The thermal loading depends on the electromagnetic properties of the TM_{01} mode as well as the length of the corrugated waveguide and the conductivity of the wall material. Achieving a high repetition rate requires active cooling of the structure as well as an optimally designed corrugation profile. Here we focus on designing a corrugation that minimizes the steady-state thermal load and transient pulse heating. The thermally induced stresses due to temperature gradients in the wall pose additional design considerations which are discussed further in [26].

Because the group velocity v_g of the electromagnetic wave is less than the electron bunch velocity, the length of the rf pulse behind the bunch grows as it traverses the structure. This causes the thermal energy density deposited in the CWG wall to increase along the direction of propagation. At a distance z from the beginning of the CWG, the field strength of the rf pulse induced by the electron bunch entering at time $t = 0$ is

$$P^{1/2}(z,t) = \sqrt{\frac{2\kappa q_0^2 |F|^2 v_g}{1-\beta_g}} e^{\frac{-\alpha(v_g t-\beta_g z)}{1-\beta_g}} \cos\left[\omega\left(t-\frac{z}{c}\right)\right] \times \Pi\left(\frac{2v_g t - z(1+\beta_g)}{2z(1-\beta_g)}\right). \tag{12}$$

Here the field strength is defined in units of $\sqrt{\mathrm{W}}$ for consistency with the units provided by CST simulation, F is the bunch form factor derived in Appendix B, q_0 is the drive bunch charge, and $\Pi(x)$ is the rectangular window function.

$$\Pi(x) = \begin{cases} 1 & |x| < 1/2 \\ 0 & \text{else} \end{cases} \tag{13}$$

The derivative of the one-dimensional energy dissipation distribution $Q_{\mathrm{diss}}(z)$ along the corrugated structure is obtained by multiplying P from Eq. (12) by the attenuation constant α and integrating the product over time from $t = 0$ to $t = \infty$ giving

$$\frac{dQ_{\mathrm{diss}}(z)}{dz} = \frac{E_{\mathrm{acc}}^2}{4\kappa}(1 - e^{-2\alpha z}), \tag{14}$$

where we have made the substitution $E_{\mathrm{acc}} = 2\kappa q_0 |F|$ as derived in Appendix B. The total energy dissipated in the CWG of the length L is obtained by integrating Eq. (14) over the length L giving

$$Q_{\mathrm{diss}} = \frac{E_{\mathrm{acc}}^2}{8\alpha\kappa}(e^{-2\alpha L} + 2\alpha L - 1). \tag{15}$$

According to Eq. (14), the amount of energy deposited on the CWG wall per unit length reaches a maximum after the electron bunch propagates a distance $z \gg 1/\alpha$. It is further convenient to approximate the CWG as a smooth cylinder of radius a and elementary area $dS = 2\pi a dz$, leading to the energy dissipation density on the cylinder wall:

$$\frac{dQ_{\mathrm{diss}}(z \to \infty)}{dS} = \frac{E_{\mathrm{acc}}^2}{8\pi a\kappa}. \tag{16}$$

Since the undulating wall of the CWG has a larger surface area per unit length than the smooth cylinder, Equation (16) is an upper bound on the average energy dissipation density in the CWG wall. From Eq. (16), we define the upper bound of the average thermal power dissipation density as

$$W = \frac{E_{\mathrm{acc}}^2 f_r}{8\pi a\kappa}. \tag{17}$$

Referring to the plot for κ in Fig. 7, the power dissipation density is reduced by minimizing the corrugation period p and maximizing the spacing parameter ξ. For structures with $p/a \lesssim 0.5$, the power dissipation density decreases with an increasing aperture ratio. This results in a trade-off between minimizing the peak surface fields and minimizing the thermal loading of the CWG, where choosing a larger aperture ratio (higher TM_{01} frequency) results in higher peak fields but less thermal power dissipation.

Using $\kappa_{\max}$ from Eq. (10) in Eq. (16), we obtain the lower bound of the energy dissipation density as

$$\frac{dQ_{\mathrm{diss}}(z \to \infty)}{dS} \geq \frac{E_{\mathrm{acc}}^2 a}{4Z_0 c}. \tag{18}$$

Here we notice the linear scaling of the energy dissipation with the minor radius, a, which helps smaller diameter structures achieve less heating per pulse and thus higher bunch repetition rates. At a gradient of $E_{\mathrm{acc}} = 90\ \mathrm{MV\,m^{-1}}$, a minor radius of $a = 1$ mm, and a repetition rate of $f_r = 20$ kHz, the minimum theoretical thermal power dissipation density on the wall of the corrugated waveguide is roughly 36 $\mathrm{W/cm^2}$. This is well within the cooling capability of single phase cooling systems using water as a working fluid, see for example [27].

In addition to the steady-state thermal load, the transient heating of the corrugation plays an important role in limiting the attainable accelerating gradient. The transient temperature rise due to pulse heating causes degradation of the surface which eventually leads to nucleation sites where electric breakdown may occur [20]. Acceptable transient temperature rise is cited in the literature as 40 K [20], above which the structure begins to incur damage. The transient ΔT at the surface is calculated from a Green's function solution of the thermal diffusion equation in one dimension with Neumann boundary conditions as [20]:

$$\Delta T(t) = \frac{2}{\rho c_\epsilon}\int_0^t \frac{dP_d}{dA}\frac{1}{\delta}\exp\left[\frac{4\alpha_d(t-t')}{\delta^2}\right] \times \mathrm{erfc}\left[\frac{2}{\delta}\sqrt{\alpha_d(t-t')}\right]dt' \tag{19}$$

where ρ is the material density, c_ϵ is the specific heat, k is the thermal conductivity, $\alpha_d = k/\rho c_\epsilon$ is the thermal diffusivity, and $\delta = 1/\sqrt{\pi f \mu \sigma}$ is the skin depth. Here, dP_d/dA, given in Eq. (A9), is the power dissipation density at the waveguide surface due to the induced currents which fall off exponentially in the wall with the skin depth δ. This equation is typically approximated by assuming that the skin depth goes to zero such that all the thermal energy is deposited on the surface of the material which simplifies the integral to

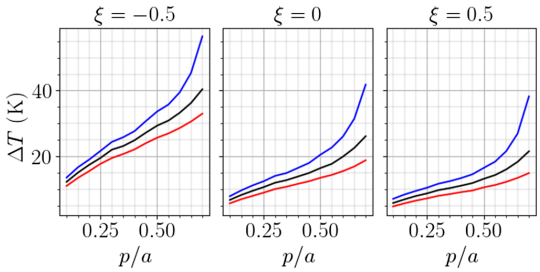

FIG. 12. Pulse heating maximum temperature rise for the maximum radii corrugation with $a=1\,\mathrm{mm}$, $E_{\mathrm{acc}}=100\,\mathrm{MV\,m^{-1}}$, and conductivity $\sigma=4\times10^{7}\ \mathrm{S\,m^{-1}}$ for $a/\lambda=0.53$ (red), $a/\lambda=0.60$ (black), and $a/\lambda=0.67$ (blue).

$$\Delta T(t)=\frac{1}{\rho c_\epsilon\sqrt{\pi\alpha_d}}\int_0^t\frac{dP_d}{dA}\frac{dt'}{\sqrt{t-t'}}. \tag{20}$$

The error in this approximation is accumulated near the beginning of the pulse when t is close to zero, causing poor accuracy when the peak temperature rise is attained quickly relative to the decay time constant of the pulse. However, the assumption that the energy is confined to the surface rather than being distributed throughout the volume guarantees that the approximation will always be an overestimate. This allows us to calculate an upper bound on ΔT by analytically evaluating the integral and maximizing the result as

$$\Delta T_{\mathrm{max}}=0.541\frac{R_s H_{\mathrm{max}}^2\sqrt{\tau}}{\rho c_\epsilon\sqrt{\pi\alpha_d}}, \tag{21}$$

where $\tau=(1-\beta_g)/2\alpha v_g$ is the decay time constant of the rf pulse and $R_s=\sqrt{\pi f\mu/\sigma}$ is the surface resistance. This result is valid when $\alpha L>0.427$ such that the maximum ΔT occurs before the end of the pulse. For pure copper at room temperature, the maximum temperature rise in K becomes

$$\Delta T_{\mathrm{max},cu}=242\frac{H_{\mathrm{max}}^2}{\sigma^{1/4}}\sqrt{\frac{f(1-\beta_g)}{\alpha_0\beta_g}} \tag{22}$$

where H_{max} is the peak surface field in $\mathrm{MA\,m^{-1}}$, f is the frequency in GHz, and α_0 is the attenuation constant in $\mathrm{Np\,m^{-1}}$ for a pure copper structure with $\sigma=5.8\times10^{7}\,\mathrm{S\,m^{-1}}$. Here, σ is the effective electrical conductivity of the structure in $\mathrm{S\,m^{-1}}$ which may be reduced from its nominal value due to surface roughness. The pulse heating depends primarily on the peak magnetic field and group velocity, having only a weak dependence on the electrical conductivity of the material. Higher group velocities lead to less pulse heating due to the shortening of the effective pulse length. Figure 12 shows how the pulse heating varies with the geometry of the maximum radii corrugation. The temperature rise, ΔT, increases with increasing corrugation period p/a and decreases with increasing spacing parameter ξ. ΔT also increases with increasing aperture ratio. The optimal corrugation design for minimal pulse heating has a small period, large spacing parameter, and small aperture ratio.

VII. HOM CONSIDERATIONS

In addition to the fundamental TM_{01} mode, the wakefield contains contributions from higher order modes (HOMs). Since the HOMs span a range of wavelengths, they may interfere either constructively or destructively with the accelerating mode at the position of the witness bunch leading to a potential reduction in the accelerating gradient. It is desirable to minimize coupling to HOMs to maintain maximum acceleration [12]. Figure 13 shows the wakefield impedance simulated with CST's wakefield solver for structures with $p/a=0.4$ (left panel) and $p/a=0.7$ (right panel), where the HOMs are seen as additional peaks in the impedance spectrum.

Characterization of the HOMs for the maximum radii structures was carried out in CST's wakefield solver by simulating 20-mm long corrugated waveguides with minor radius $a=1$ and an on-axis Gaussian bunch with standard deviation length of $\sigma_s=0.2$ mm. This bunch length resolves the wake impedance up to 500 GHz, capturing a large portion of the HOM spectrum which falls off with frequency. The sum of the loss factors for all modes is calculated as

$$\kappa_{\mathrm{tot}}=\sum\kappa_n=\frac{2}{L}\int_0^\infty \mathrm{Re}\{Z_{\|}(f)\}df, \tag{23}$$

where $Z_{\|}$ is the longitudinal wakefield impedance and L is the length of the structure. The HOM content can be characterized by the sum of HOM loss factors over the sum of all loss factors:

$$\text{HOM ratio}=\frac{\kappa_{\mathrm{tot}}-\kappa}{\kappa_{\mathrm{tot}}}, \tag{24}$$

where κ is the loss factor of the TM_{01} mode. In this characterization, the HOM ratio goes to 0 as the HOMs

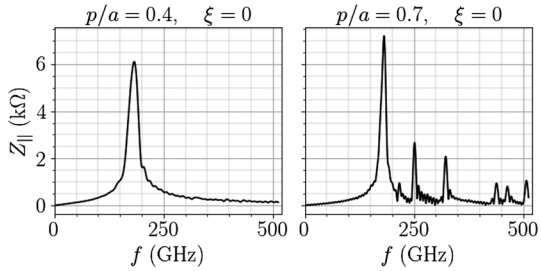

FIG. 13. Comparison of wake impedance for maximum radii structures with $p/a=0.4$ (left panel) and $p/a=0.7$ (right panel) and aperture ratio $a/\lambda=0.60$. The HOMs are seen as additional peaks for the larger period structure on the right.

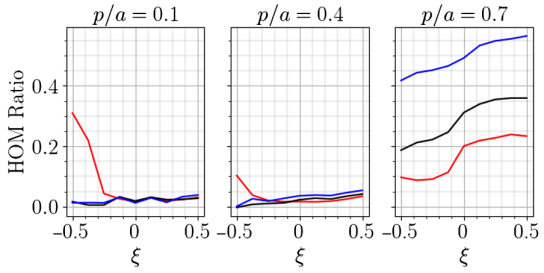

FIG. 14. Ratio of the HOM wakefield to the total wakefield for an impulse excitation with $a/\lambda = 0.53$ (red), $a/\lambda = 0.60$ (black), and $a/\lambda = 0.67$ (blue).

vanish, at which point the loss is due exclusively to the TM_{01} mode. Figure 14 shows that the HOM content primarily depends on the corrugation period, where periods larger than $0.4a$ lead to significant HOM coupling. The HOMs also increase modestly with aperture ratio and corrugation spacing. The HOM ratio shown here assumes that all modes are excited equally which is not the case for a finite length bunch with a limited charge spectrum. The actual HOM energy content must account for the bunch shape by inclusion of the form factor discussed in Appendix B.

VIII. CORRUGATED WAVEGUIDE DESIGN FOR A-STAR

Guided by the preceding analysis of peak fields, thermal loading, and HOM coupling, we now present the CWG design for the A-STAR accelerator under development at Argonne National Laboratory. The dimensions of the structure, shown in Fig. 15, are selected to maximize E_{acc} and f_r by maintaining manageable thermal loading, peak surface fields, and manufacturability. Experimental measurement of the breakdown rate is required to determine the maximum accelerating gradient.

The first step in the design process is to choose the minor radius, a, of the CWG which determines the maximum value of the loss factor κ according to Eq. (10). In choosing a, the beam breakup instability (BBU) caused by the transverse momentum kick on the particles in the tail of the bunch when the leading particles traverse the CWG off-axis has to be considered (see [28] and references therein). Because the kick factor associated with the BBU scales as a^{-4} [18], the minimum radius of the structure and corresponding maximum loss factor κ are ultimately determined by beam stability constraints. Simulations show that reducing a below 1 mm may result in the onset of BBU under certain conditions.

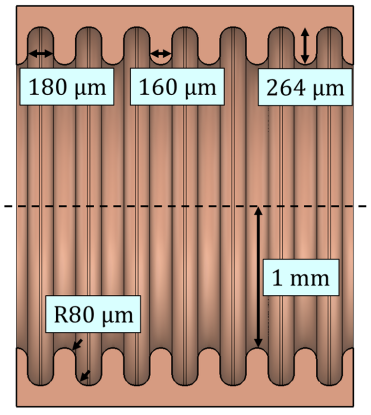

FIG. 15. A-STAR CWG dimensions.

After determining the minor radius, a, of 1 mm, the frequency and corresponding aperture ratio of the synchronous TM_{01} accelerating mode must be chosen. We have shown in Figs. 10 and 12 that the peak surface fields and associated pulse heating increase with aperture ratio while the total power dissipation decreases, as shown by its dependence on the loss factor κ in Eq. (16) and Fig. 7. In addition to these considerations, the frequency must be compatible with the electromagnetic output couplers used to extract rf energy from the structure. An important feature of A-STAR is its ability to measure the trajectory of the bunch in the CWA using the HEM_{11} mode which is excited when the beam propagates off-axis. Due to mode conversion, the design of the coupler that extracts the HEM_{11} mode becomes increasingly challenging as the HEM_{11} wavelength shrinks with respect to the fixed aperture of the waveguide. For the 1-mm minor radius cylindrical waveguide, the limiting factor in the HEM_{11} coupler design was converted to the TE_{31} mode which has a cutoff frequency of 200 GHz. To address this, the synchronous HEM_{11} mode was chosen to be 10 GHz below the TE_{31} cutoff frequency, resulting in a 190-GHz HEM_{11} mode and 180-GHz TM_{01} mode with an aperture ratio of $a/\lambda = 0.60$.

With the minor radius and frequency selected, the corrugation profile is chosen to maximize the accelerating gradient as well as provide a high repetition rate. The 1-mm minor radius of the CWG results in corrugation dimensions in the hundreds of μm which presents unique manufacturing challenges. Several fabrication methods have been investigated for constructing the CWG, with electroforming copper on an aluminum mandrel producing the most promising results [14]. Electroforming at these scales requires that neither the corrugation tooth width nor the vacuum gap is made excessively small since this would result in either a flimsy mandrel or a flimsy final structure. A sensible choice is to make the tooth width similar to the vacuum gap, resulting in $\xi \approx 0$, while using the shortest practical corrugation period. The maximum radii and unequal radii geometries have similar characteristics when $\xi \approx 0$ and we have selected the maximum radii design for A-STAR. The final corrugation dimensions are shown in Table II and the electromagnetic characteristics of the TM_{01} and HEM_{11} modes are given in Table III.

Maintaining the fundamental TM_{01} and HE_{11} frequencies within a ± 5 GHz-bandwidth specified by the design of

TABLE II. A-STAR key operating parameters.

Parameter		
a	1 mm	Corrugation minor radius
d	264 μm	Corrugation depth
g	180 μm	Corrugation vacuum gap
t	160 μm	Corrugation tooth width
$r_{t,g}$	80 μm	Corrugation corner radius
p	340 μm	Corrugation period
ξ	0.06	Spacing parameter
L	50 cm	Waveguide module length
$\mathcal{R}$	5	Transformer ratio
$\lvert F\rvert$	0.382	Bunch form factor
q_0	10 nC	Bunch charge
E_{acc}	90 MV m^{-1}	Accelerating gradient
E_{max}	325 MV m^{-1}	Peak surface E field
H_{max}	610 kA m^{-1}	Peak surface H field
ϕ	74°	Phase advance
f_r	20 kHz	Repetition rate
P_{diss}	1050 W	Power dissipation per module
W	55 W/cm^2	Power density upper bound
ΔT	9.5 K	Pulse heating

the output couplers requires dimensional tolerances of roughly ±10 μm, as shown by Fig. 5. The most sensitive dimension to manufacturing error is the corrugation depth, which must be carefully controlled to produce the desired frequency. Mode conversion due to the straightness of the CWG is not expected to change the acceleration properties over the short length scale between the drive and witness bunch. However, such effects may become relevant in the operation of the output couplers and are a subject of future analysis.

The A-STAR design is made up of 0.5-m long CWG modules connected in series by 40-mm long transition sections which contain the rf output couplers, vacuum pumping ports, and bellows. The addition of the transition sections increases the overall length of the accelerator by less than 10%. The transformer ratio $\mathcal{R}$ is determined by the longitudinal charge density of the drive bunch $q(s)$, where it has been shown in [12] that $\mathcal{R}$ can be maximized by using a "doorstep" type charge distribution defined as

$$q(s) = N \times \begin{cases} 1 & 0 < s < \pi/(2k_n) \\ k_n s + (1 - \pi/2) & \pi/(2k_n) < s < l \\ 0 & \text{else} \end{cases} \quad (25)$$

where s is the longitudinal displacement from the head of the bunch, $k_n = \omega_n/c$ is the wave number of the TM_{01} mode, $l = (\sqrt{\mathcal{R}^2 - 1} + \pi/2 - 1)/k_n$ is the bunch length, and $N = 2k_n q_0/(\mathcal{R}^2 + \pi - 2)$ is a normalization constant such that $\int q(s)ds = q_0$ is the total charge of the bunch. The accelerating wakefield behind the drive bunch is given by the convolution of the charge density $q(s)$ with the Green's function of the structure $h(s)$ and can be calculated from Eqs. (26) and (27), and Eq. (B3), resulting in the accelerating field shown in Fig. 16 for the A-STAR design.

$$E_z(s) = \int_{-\infty}^{\infty} q(s - s')h(s')ds' \quad (26)$$

$$h(s) = \sum_{n=0}^{\infty} 2\kappa_n \cos(k_n s)\theta(s). \quad (27)$$

The wakefield falls off exponentially behind the drive bunch due to ohmic loss in the wall material, leading to an rf pulse power envelope at the end of a half-meter section of A-STAR resembling that in Fig. 17. In the copper structure, the trailing edge of the power envelope is attenuated by 85% after a half meter. For structures longer than $\sim 1/\alpha$, the pulse length becomes saturated and is determined by the conductivity of the wall material rather than the length of the CWG, where lower conductivity produces a shorter pulse. Because the witness bunch follows close behind the drive bunch, the loss in accelerating gradient for a lossy wall CWG can be small while the overall thermal load remains unchanged according to Eq. (16). This feature of the CWA can potentially be exploited to allow fabrication from lossy materials or use of surface coatings to improve

TABLE III. A-STAR synchronous electromagnetic mode characteristics. The loss factor κ for the HEM_{11} mode scales with the square of the beam offset and is given for the offset of 1 μm. The attenuation coefficient α is given for a structure with the conductivity of 4×10^7 S m^{-1}.

	TM_{01}	HEM_{11}	Units
f	180	190	GHz
κ	1.18×10^{16}	2.19×10^{10}	V C^{-1} m^{-1}
β_g	0.57	0.62	None
α	2.31	1.96	Np m^{-1}

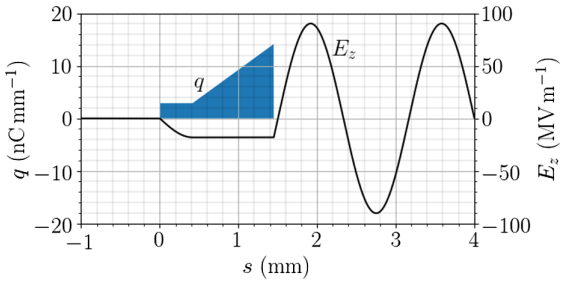

FIG. 16. A 10-nC doorstep charge distribution and resulting wake potential of the TM_{01} mode for the A-STAR CWG, showing a transformer ratio $\mathcal{R} = 5$ and peak accelerating gradient $E_{\mathrm{acc}} = 90$ MV m^{-1}.

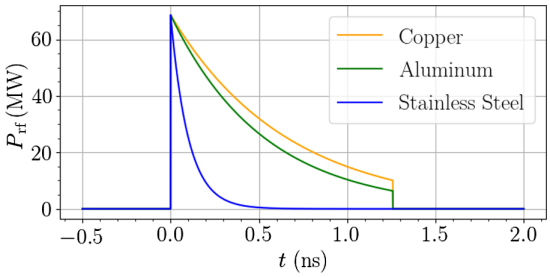

FIG. 17. rf power envelope at the end of a 0.5-m section of the A-STAR CWG made from copper (5.8×10^7 S m^{-1}), aluminum (3.8×10^7 S m^{-1}), and stainless steel (1.35×10^6 S m^{-1}).

performance. The reduction in pulse length may be used as a way to increase the rf breakdown threshold of the structure.

IX. CONCLUSION

Through simulation, we have shown how the electromagnetic parameters characterizing the TM_{01} synchronous mode of a cylindrical CWG used as a slow-wave structure depend on the corrugation period, spacing, sidewall angle, and frequency of the accelerating mode. In analyzing the structures, we found that minimizing the corrugation period plays a key role in reducing the peak electromagnetic fields, thermal loading, and coupling to HOMs. Taking into account electromagnetic and manufacturing considerations, we found the most practical corrugation profile has vertical sidewalls and a corrugation tooth width similar to the width of the vacuum gap. Using the results of our analysis, we have designed a prototype CWG for the A-STAR CWA under development at Argonne National Laboratory. The calculated parameters of A-STAR suggest that a CWA based on a metallic corrugated waveguide is a promising approach to realize a new generation of high repetition rates and compact XFEL light sources.

ACKNOWLEDGMENTS

This manuscript is based upon work supported by Laboratory Directed Research and Development (LDRD) funding from Argonne National Laboratory (ANL), provided by the Director, Office of Science, of the U.S. Department of Energy under Contract No. DE-AC02-06CH11357. Useful discussions with W. Jansma, S. Lee, A. Nassiri, B. Popovic, J. Power, S. Sorsher, K. Suthar, E. Trakhtenberg, and J. Xu of ANL are gratefully acknowledged.

APPENDIX A: SCALING AND NORMALIZATION

Here, we derive the scaling laws for the loss factor κ, group velocity β_g, and attenuation constant α. We will assume that σ satisfies the conditions of a good conductor so that the field solutions are independent of conductivity. The time harmonic eigenmode solutions $\boldsymbol{E}$ and $\boldsymbol{H}$ produced by CST are normalized such that the stored energy U in the unit cell is 1 J and the frequency is ω. Uniformly scaling the geometry by a constant $\hat{a}$ while holding the stored energy fixed results in the scaled eigenmode solutions:

$$\begin{aligned}\boldsymbol{E}'(x,y,z)e^{j\omega' t} &= \hat{a}^{-3/2}\boldsymbol{E}(x',y',z')e^{j\omega\frac{t}{\hat{a}}}\\ \boldsymbol{H}'(x,y,z)e^{j\omega' t} &= \hat{a}^{-3/2}\boldsymbol{H}(x',y',z')e^{j\omega\frac{t}{\hat{a}}},\end{aligned} \tag{A1}$$

where

$$x' = \frac{x}{\hat{a}}, \qquad y' = \frac{y}{\hat{a}}, \qquad z' = \frac{z}{\hat{a}}, \qquad \omega' = \frac{\omega}{\hat{a}}. \tag{A2}$$

Scaling the fields by $\hat{a}^{-3/2}$ keeps the stored energy U' of the scaled structure same as that of the unscaled structure U, which is seen by integrating the total energy in the fields:

$$\begin{aligned}U' &= \iiint \frac{\epsilon_0}{2}|\hat{a}^{-3/2}\boldsymbol{E}(x',y',z')|^2\\ &\quad + \frac{\mu_0}{2}|\hat{a}^{-3/2}\boldsymbol{H}(x',y',z')|^2 dxdydz\\ &= \iiint \frac{\epsilon_0}{2}|\boldsymbol{E}(x',y',z')|^2\\ &\quad + \frac{\mu_0}{2}|\boldsymbol{H}(x',y',z')|^2 dx'dy'dz' = U,\end{aligned} \tag{A3}$$

where the integrals are over all space. Applying the normalized fields with $U = 1$ to Eq. (8) for the group velocity shows that group velocity is independent of scaling

$$\begin{aligned}v_g' &= \hat{a}p\iint \frac{1}{2}\mathrm{Re}\{\boldsymbol{E}'(x,y)\times\boldsymbol{H}'^*(x,y)\}dxdy\\ &= p\iint \frac{1}{2}\mathrm{Re}\{\boldsymbol{E}(x',y')\times\boldsymbol{H}^*(x',y')\}dx'dy' = v_g.\end{aligned} \tag{A4}$$

Using Eq. (7), the induced voltage V' in the scaled structure is

$$V' = \left|\int_0^{\hat{a}p} \hat{a}^{-3/2}E_z(z')e^{j\omega'\frac{z}{c}}dz\right|, \tag{A5}$$

which can be written as

$$V' = \left|\int_0^{p} \hat{a}^{-1/2}E_z(z')e^{j\omega\frac{z'}{c}}dz'\right| = \frac{V}{\hat{a}^{1/2}}. \tag{A6}$$

Since we have normalized the fields with $U = 1$ J and shown that the group velocity β_g is independent of scaling, Equation (6) is used to write the loss factor for the scaled structure as

$$\kappa' = \frac{V'^2/U}{4(1-\beta_g)\hat{a}p} = \frac{\kappa}{\hat{a}^2}. \tag{A7}$$

The quality factor Q of the corrugation unit cell is defined as

$$Q = \frac{\omega U}{P_d}, \tag{A8}$$

where U is stored energy and P_d is the power dissipated in the cavity walls. The power dissipation density per unit area is

$$\frac{dP_d}{dA} = \frac{1}{2}\sqrt{\frac{\omega\mu}{2\sigma}}|\boldsymbol{H}|^2. \tag{A9}$$

In the scaled structure, the power dissipation and resulting quality factor become

$$P'_d = \hat{a}^{-3/2}P_d, \qquad Q' = \hat{a}^{1/2}Q, \tag{A10}$$

leading to the scaled attenuation constant from Eq. (9)

$$\alpha' = \hat{a}^{-3/2}\alpha. \tag{A11}$$

Scaling of the attenuation constant α with conductivity is accomplished by multiplying α by $\sqrt{\sigma/\sigma'}$ where σ is the conductivity of the unscaled structure and σ' is the conductivity of the scaled structure.

APPENDIX B: BUNCH FORM FACTOR DERIVATION

When calculating a bunch's energy loss to a particular mode of the corrugated waveguide, the shape of the bunch described by the bunch peak current distribution $i(t)$ is accounted for by scaling the loss factor κ by the Fourier transform $I(\omega_n)$ of the current, where ω_n is the angular frequency of the synchronous mode. The form factor $F(k_n)$ of the bunch is defined as $I(\omega_n)/q_0$, where k_n is the wave number of the synchronous mode and q_0 is the total charge of the bunch. Here, time t begins when the head of the bunch passes a fixed observation point in the corrugated waveguide. We begin by considering the kinetic energy lost by an element of charge idt as it moves a distance cdt in an electric field E_z:

$$d^2U_{\text{loss}} = (idt)(cdt)E_z. \tag{B1}$$

Here, the electric field E_z is the wakefield left behind by the current in the head of the bunch which has already passed the observation point. The wakefield produced by a current impulse $q_0\delta(t)$ is the Green's function $h(t)$ which is expressed as an expansion over the normal modes of the corrugation unit cell as

$$h(t) = \sum_{n=0}^{\infty} 2\kappa_n \cos(\omega_n t)\theta(t), \tag{B2}$$

where $\theta(t)$ is the Heaviside theta function

$$\theta(t) = \begin{cases} 0 & t < 0 \\ 1/2 & t = 0 \\ 1 & t > 0 \end{cases} \tag{B3}$$

and κ_n is the loss factor given in Eq. (6) in units of $\mathrm{V\,m^{-1}\,C^{-1}}$. The fields in the unit cell are time harmonic, oscillating with frequency ω_n. Because the structure is approximated to be periodic, the oscillating fields are part of an infinitely long traveling wave that never decays. In terms of the Green's function $h(t)$, the wakefield $E_z(t)$ due to the total current distribution $i(t)$ is then constructed with the convolution integral

$$E_z(t) = \int_{-\infty}^{\infty} h(t-t')i(t')dt'. \tag{B4}$$

Inserting Eq. (B4) into Eq. (B1) and integrating over the time axis of the bunch produce the power being deposited into the wakefield

$$P_w = \frac{dU_{\text{loss}}}{dt} = c\int_{-\infty}^{\infty} i(t)\int_{-\infty}^{\infty} h(t-t')i(t')dt'dt. \tag{B5}$$

Defining the Fourier transform and its inverse

$$I(\omega) = \int_{-\infty}^{\infty} i(t)e^{-j\omega t}dt, \tag{B6}$$

$$i(t) = \frac{1}{2\pi}\int_{-\infty}^{\infty} I(\omega)e^{j\omega t}d\omega. \tag{B7}$$

Equation (B5) can now be written in terms of the Fourier transformed functions as

$$P_w = \frac{c}{(2\pi)^3}\mathrm{Re}\left\{\int_{-\infty}^{\infty}\int_{-\infty}^{\infty} I(\omega_2)e^{j\omega_2 t}d\omega_2\int_{-\infty}^{\infty} \times \int_{-\infty}^{\infty} I(\omega_1)e^{j\omega_1(t-t')}d\omega_1\int_{-\infty}^{\infty} Z_{||}(\omega)e^{j\omega t'}d\omega dt'dt\right\}. \tag{B8}$$

Here we have used the convolution's commutative property to switch the roles of i and h in the convolution integral and written the Fourier transform of Green's function $h(t)$ as the longitudinal wake impedance $Z_{||}(\omega)$. The subscripts added to the ω variables indicate that they are independent, allowing Eq. (B8) to be rearranged:

$$P_w = \frac{c}{(2\pi)^3}\mathrm{Re}\left\{\int_{-\infty}^{\infty} d\omega \int_{-\infty}^{\infty} d\omega_2 \int_{-\infty}^{\infty} d\omega_1 \int_{-\infty}^{\infty} dt \int_{-\infty}^{\infty} dt' \times I(\omega_2) I(\omega_1) Z_{||}(\omega) e^{jt(\omega_1+\omega_2)} e^{jt'(\omega-\omega_1)}\right\}. \quad \text{(B9)}$$

The integrals in t and t' produce Dirac delta functions leaving

$$P_w = \frac{c}{2\pi}\mathrm{Re}\left\{\int_{-\infty}^{\infty} d\omega \int_{-\infty}^{\infty} d\omega_2 \int_{-\infty}^{\infty} d\omega_1 \times I(\omega_2) I(\omega_1) Z_{||}(\omega) \delta(\omega_1+\omega_2)\delta(\omega-\omega_1)\right\}. \quad \text{(B10)}$$

Using the sifting property of the delta function to evaluate the integral Eq. (B10) becomes

$$P_w = \frac{c}{2\pi}\mathrm{Re}\left\{\int_{-\infty}^{\infty} I(-\omega) I(\omega) Z_{||}(\omega) d\omega\right\}. \quad \text{(B11)}$$

Since the current density $i(t)$ is a purely real function, $I(-\omega) = I^*(\omega)$ where * denotes complex conjugation, leading to

$$P_w = \frac{c}{2\pi}\int_{-\infty}^{\infty} |I(\omega)|^2 \,\mathrm{Re}\{Z_{||}(\omega)\} d\omega. \quad \text{(B12)}$$

Equation (B12) represents the power being converted from kinetic energy to electromagnetic energy in the frequency domain. Considering a single mode denoted by the subscript n, the wake impedance is

$$Z_{n||}(\omega) = \int_{-\infty}^{\infty} 2\kappa_n \cos(\omega_n t)\theta(t) e^{-j\omega t} dt. \quad \text{(B13)}$$

Using the Fourier transform property

$$\mathcal{F}\{f(t)\cos(at)\} = \frac{F(\omega-a)+F(\omega+a)}{2}, \quad \text{(B14)}$$

and the Fourier transform of the step function

$$\mathcal{F}\{\theta(t)\} = \pi\left(\frac{1}{j\pi\omega} + \delta(\omega)\right), \quad \text{(B15)}$$

the wake impedance becomes

$$Z_{n||}(\omega) = \kappa_n\left[\pi[\delta(\omega-\omega_n)+\delta(\omega+\omega_n)] - j\left(\frac{1}{(\omega-\omega_n)}+\frac{1}{(\omega+\omega_n)}\right)\right]. \quad \text{(B16)}$$

Using $Z_{n||}(\omega)$ in Eq. (B12) and evaluating the integral yields

$$P_{w,n} = \frac{\kappa_n c}{2}(|I(\omega_n)|^2 + |I(-\omega_n)|^2). \quad \text{(B17)}$$

Again, using the fact that the current distribution is a purely real function, we obtain

$$P_{w,n} = \kappa_n c |I(\omega_n)|^2. \quad \text{(B18)}$$

Assuming the loss factor κ_n is uniform throughout the corrugated waveguide of length L, the total energy lost by the bunch to the wakefield mode is

$$U_{\mathrm{loss},n} = \kappa_n L |I(\omega_n)|^2 \quad \text{(B19)}$$

In terms of the bunch form factor, $F(k)$ is defined as

$$F(k) = \frac{1}{q_0}\int_{-\infty}^{\infty} q(s) e^{-jks} ds, \quad \text{(B20)}$$

where s is the longitudinal displacement from the head of the bunch and k is the wave number, the energy loss is

$$U_{\mathrm{loss},n} = \kappa_n q_0^2 |F(k_n)|^2. \quad \text{(B21)}$$

We will now consider the effect of the bunch charge density $q(s)$ on the accelerating field $E_z(s)$ in order to understand how E_{acc} and the peak surface fields depend on $q(s)$. To begin, we write $E_{z,n}$ due to a single mode as a convolution

$$E_{z,n}(s) = \int_{-\infty}^{\infty} q(s-s') 2\kappa_n \cos(k_n s')\theta(s') ds'. \quad \text{(B22)}$$

Since $q(s)$ is a real function,

$$E_{z,n}(s) = 2\kappa_n \mathrm{Re}\left\{\int_0^{\infty} q(s-s') e^{jk_n s'} ds'\right\}. \quad \text{(B23)}$$

Making the substitution $u = s - s'$,

$$E_{z,n}(s) = 2\kappa_n \mathrm{Re}\left\{\int_{-\infty}^{s} q(u) e^{jk_n(s-u)} du\right\}. \quad \text{(B24)}$$

Since we are only interested in the fields behind the bunch, we take the limit as $s \to \infty$, noting that the result will be valid outside the bunch where $q(s) = 0$:

$$E_{z,n}(s\to\infty) = 2\kappa_n \mathrm{Re}\left\{e^{jk_n s}\int_{-\infty}^{\infty} q(u) e^{-jk_n u} du\right\}. \quad \text{(B25)}$$

We can now write the field in terms of the previously derived form factor $F(k_n)$ given in Eq. (B20):

$$E_{z,n}(s \to \infty) = 2\kappa_n q_0 \mathrm{Re}\{e^{jk_n s} F(k_n)\} \tag{B26}$$

Expanding the real part

$$E_{z,n}(s \to \infty) = 2\kappa_n q_0 [\cos(k_n s)\mathrm{Re}\{F(k_n)\} - \sin(k_n s)\mathrm{Im}\{F(k_n)\}]. \tag{B27}$$

Since we are interested in the maximum value of the longitudinal accelerating field, we define E_{acc} as the amplitude of $E_{z,n}(s \to \infty)$:

$$E_{\mathrm{acc}} = 2\kappa q_0 \sqrt{\mathrm{Re}\{F(k_n)\}^2 + \mathrm{Im}\{F(k_n)\}^2} \tag{B28}$$

which reduces to

$$E_{\mathrm{acc}} = 2\kappa q_0 |F(k_n)| \tag{B29}$$

For the doorstep distribution of Eq. (25) with transformer ratio $\mathcal{R}$ and wave number $k_n = \omega_n/c$, the form factor $|F(k)|$ is calculated from Eq. (B20) as

$$|F(k)| = \frac{2k_n}{\mathcal{R}^2 + \pi - 2}\left\{\frac{\mathcal{R}^2}{k^2} + \frac{2k_n}{k^3}\left[\frac{k_n}{k}\left[1 - \cos\left(kl - \frac{\pi k}{2k_n}\right)\right] + \sin(kl) - \sin\left(\frac{\pi k}{2k_n}\right)\right] - \frac{2}{k^2}\sqrt{\mathcal{R}^2 - 1}\left[\cos(kl) + \frac{k_n}{k}\sin\left(kl - \frac{\pi k}{2k_n}\right)\right]\right\}^{1/2}, \tag{B30}$$

where the bunch length l is

$$l = \frac{\frac{\pi}{2} + \sqrt{\mathcal{R}^2 - 1} - 1}{k_n}. \tag{B31}$$

Evaluating the form factor at $k = k_n$ produces

$$|F(k_n)| = \frac{2\mathcal{R}}{\mathcal{R}^2 + \pi - 2}. \tag{B32}$$

This result leads to the accelerating gradient E_{acc} scaling with the inverse of the transformer ratio $\mathcal{R}$.

[1] A. Zholents, S. Baturin, D. Doran, W. Jansma, M. Kasa, A. Nassiri, P. Piot, J. Power, A. Siy, S. Sorsher, K. Suthar, W. Tan, E. Trakhtenberg, G. Waldschmidt, and J. Xu, A compact high repetition rate free-electron laser based on the Advanced Wakefield Accelerator Technology, in *Proceedings of the 11th International Particle Accelerator Conference, IPAC-2020, CAEN, France* (2020), https://ipac2020.vrws.de/html/author.htm.

[2] A. Zholents *et al.*, A conceptual design of a compact wakefield accelerator for a high repetition rate multi user X-ray Free-Electron Laser Facility, in *Proceedings of the 9th International Particle Accelerator Conference, IPAC'18, Vancouver, BC, Canada* (JACoW Publishing, Geneva, Switzerland, 2018), pp. 1266–1268, 10.18429/JACoW-IPAC2018-TUPMF010.

[3] G. Voss and T. Weiland, The wake field acceleration mechanism, DESY Technical Report No. DESY-82-074, 1982.

[4] R. J. Briggs, T. J. Fessenden, and V. K. Neil, Electron autoacceleration, in *Proceedings of the 9th International Conference on the High-Energy Accelerators, Stanford, CA, 1974* (A.E.C., Washington, DC, 1975), p. 278

[5] M. Friedman, Autoacceleration of an Intense Relativistic Electron Beam, Phys. Rev. Lett. **31**, 1107 (1973).

[6] E. A. Perevedentsev and A. N. Skrinsky, On the use of the intense beams of large proton accelerators to excite the accelerating structure of a linear accelerator, in *Proceedings of 6th All-Union Conference Charged Particle Accelerators, Dubna* (Institute of Nuclear Physics, Novosibirsk, USSR, 1978), Vol. 2, p. 272; English version is available in *Proceedings of the 2nd ICFA Workshop on Possibilities and Limitations of Accelerators and Detectors, Les Diablerets, Switzerland, 1979* (CERN, Geneva, Switzerland,1980), p. 61

[7] Y. Chin, The wake field acceleration using a cavity of elliptical cross section, in *Proceedings of the 12th International Linac Conference, LINAC-1984, Seeheim, Germany, 1984* (GSI, Darmstadt, Germany, 1984), pp. 159–161.

[8] W. Gai, P. Schoessow, B. Cole, R. Konecny, J. Norem, J. Rosenzweig, and J. Simpson, Experimental Demonstration of Wakefield Effects in Dielectric Structures, Phys. Rev. Lett. **61**, 2756 (1988).

[9] I. Syratchev, D. Schulte, E. Adli, and M. Taborelli, High RF power production for CLIC, in *Proceedings of the 22nd Particle Accelerator Conference, PAC-2007, Albuquerque, NM, 2007* (IEEE, New York, 2007), pp. 2194–2196, https://accelconf.web.cern.ch/p07/PAPERS/WEPMN071.PDF.

[10] K. L. Bane, P. Chen, and P. B. Wilson, On collinear wake field acceleration, *Proceedings of the 11th Particle Accelerator Conference, PAC-1985, Vancouver, BC, Canada, 1985* (IEEE, New York, 1985), Vol. 32, p. 3524.

[11] W. H. Tan, P. Piot, and A. Zholents, Formation of temporally shaped electron bunches for beam-driven collinear wakefield accelerators, Phys. Rev. Accel. Beams **24**, 051303 (2021).

[12] S. S. Baturin and A. Zholents, Upper limit for the accelerating gradient in the collinear wakefield accelerator as a function of the transformer ratio, Phys. Rev. Accel. Beams **20**, 061302 (2017).

[13] CST Microwave Studio, Dassault Systems, Inc. (2020).

[14] A. Siy, N. Behdad, J. Booske, M. Fedurin, W. Jansma, K. Kusche, S. Lee, G. Mouravieff, A. Nassiri, S. Oliphant, S. Sorsher, K. Suthar, E. Trakhtenberg, G. Waldschmidt, and A. Zholents, Fabrication and testing of corrugated waveguides for a collinear wakefield accelerator, Phys. Rev. Accel. Beams **25**, 021302 (2022).

[15] K. Suthar, E. Trakhtenberg, S. Sorsher, and A. Zholents, Vacuum analysis of a corrugated waveguide wakefield

accelerator, *Proceedings of MEDSI2020*, p. 160, https://accelconf.web.cern.ch/medsi2020/papers/tupb07.pdf.

[16] V. Dolgashev and S. Tantawi, Design of high efficiency high power electron accelerator systems based on normal conducting RF technology for energy and environmental applications, design study report, SLAC National Accelerator Laboratory (2018), pp. 4–18, 10.2172/1441166.

[17] W. Thomas, *RF Linear Accelerators*, 2nd ed. (Wiley-VCH, New York, 2008).

[18] K. Bane and G. Stupakov, Corrugated pipe as a beam dechirper, Nucl. Instrum. Methods Phys. Res., Sect. A **690**, 106 (2012).

[19] M. Dal Forno, V. Dolgashev, G. Bowden, C. Clarke, M. Hogan, D. McCormick, A. Novokhatski, B. Spataro, S. Weathersby, and S. G. Tantawi, Experimental measurements of rf breakdowns and deflecting gradients in mm-wave metallic accelerating structures, Phys. Rev. Accel. Beams **19**, 051302 (2016).

[20] D. P. Pritzkau and R. H. Siemann, Experimental study of rf pulsed heating on oxygen free electronic copper, Phys. Rev. ST Accel. Beams **5**, 112002 (2002).

[21] A. Grudiev and W. Wuensch, A new local field quantity describing the high gradient limit of accelerating structures, in *Proceedings of the 24th Linear Accelerator Conference, LINAC 2008, Victoria, BC, Canada* (TRIUMF, Victoria, BC, Canada, 2008), Vol. 102001, p. 936.

[22] M. Dal Forno, V. Dolgashev, G. Bowden, C. Clarke, M. Hogan, D. McCormick, A. Novokhatski, B. Spataro, S. Weathersby, and S. G. Tantawi, rf breakdown tests of mm-wave metallic accelerating structures, Phys. Rev. Accel. Beams **19**, 011301 (2016).

[23] M. Dal Forno, V. Dolgashev, G. Bowden, C. Clarke, M. Hogan, D. McCormick, A. Novokhatski, B. O'Shea, B. Spataro, S. Weathersby, and S. G. Tantawi, rf breakdown measurements in electron beam driven 200 GHz copper and copper-silver accelerating structures, Phys. Rev. Accel. Beams **19**, 111301 (2016).

[24] E. I. Simakov, V. A. Dolgashev, and S. G. Tantawi, Advances in high gradient normal conducting accelerator structures, Nucl. Instrum. Methods Phys. Res., Sect. A **907**, 221 (2018).

[25] V. Dolgashev, S. Tantawi, Y. Higashi, and B. Spataro, Geometric dependence of radio-frequency breakdown in normal conducting accelerating structures, Appl. Phys. Lett. **97**, 171501 (2010).

[26] K. Suthar, A. Siy, G. J. Waldschmidt, S. Lee, S. Sorsher, E. Trakhtenberg, and A. Zholents, Determination of maximum repetition rate of a corrugated-waveguide-based wakefield accelerator, *Proceedings of MEDSI2020* (2020), Vol. 336, https://accelconf.web.cern.ch/medsi2020/papers/thio02.pdf.

[27] M. A. Ebadian and C. X. Lin, A review of high-heat-flux heat removal technologies, J. Heat Transfer **133**, 1 (2011).

[28] S. S. Baturin and A. Zholents, Stability condition for the drive bunch in a collinear wakefield accelerator, Phys. Rev. Accel. Beams **21**, 031301 (2018).